Constraining the 410-km Discontinuity with Triplication Waveform

submitted to *Geophys. J. Int.*

Constraining the 410-km Discontinuity with Triplication Waveform

Jiaqi Li [1⋆], Min Chen [1,2], Jieyuan Ning [3], Tiezhao Bao [3], Ross Maguire [1,4] and Tong Zhou [5]

[1] *Department of Computational Mathematics, Science and Engineering, Michigan State University, East Lansing, Michigan* 48824*, USA. E-mail: lijiaqi9@msu.edu*

[2] *Department of Earth and Environmental Sciences, Michigan State University, East Lansing, Michigan* 48824*, USA.*

[3] *School of Earth and Space Sciences, Peking University, Beijing* 100871*, China.*

[4] *Department of Earth and Planetary Sciences, University of New Mexico, Albuquerque, NM,* 87131*, USA.*

[5] *Earth, Planetary and Space Sciences, University of California Los Angeles, CA,* 90095*, USA.*

SUMMARY

The detailed structures near the 410-km discontinuity provide key constraints of the dynamic interactions between the upper mantle and the lower mantle through the mantle transition zone via mass and heat exchange. The 410-km discontinuity topography inside the slab could be used to infer the existence of the metastable olivine wedge, further investigate the possible mechanism for deepfocus earthquakes. Multipathing, i.e., triplicated, body waves that bottom near the 410-km discontinuity carry rich information of this discontinuity, such as interface depth and wave speed jump across it. In this study, we first systematically analyze the tradeoff between

model parameters in triplication studies. Additionally, we illustrate the necessity of using array normalized amplitude. Finally, with the non-gradient-based inversion package we have developed, we derived a 1-D depth profile of the wave speed below the Tatar Strait of Russia. We have observed triplications for both the 410-km discontinuity and the slab upper surface, and simultaneously derived seismic structures for these two interfaces. The upper surface of the slab is located at 480±10 km, which is consistent with the location of the 1% wave speed contour of the regional tomography results, but with a larger amplitude. This significant wave speed jump of $\sim$ 7% is contributed by both the differences across the slab upper surface and a low wave speed anomaly above the subducting slab. The 410-km discontinuity is located at 410±5 km, indicating little thermal influence from the distant subducting slab located $\sim$ 70 km below it.

Key words: 410-km discontinuity; triplication; tradeoff; non-gradient-based inversion; subducting slab

1 INTRODUCTION

The 410-km discontinuity marks the top of the mantle transition zone (MTZ). This interface represents the mineralogical phase change of olivine to wadsleyite at around 410 km, demonstrated by laboratory experiments (Ringwood 1975). The detailed structures near the 410-km discontinuity provide key constraints of the dynamic interactions between the upper mantle and the lower mantle through the MTZ via mass and heat exchange.

One of the essential interactions involves cold slabs penetrating and elevating the 410-km discontinuity and carrying volatiles into the transition zone (Kawakatsu & Watada 2007). At this pressure-temperature induced phase transition interface, the pressure (depth) and the temperature is one-to-one correlated. Therefore, the 410-km discontinuity depth provides an in situ thermometer near the top of the mantle transition zone. The 410-km discontinuity thickness (sharpness) is sensitive to the water content (Helffrich & Wood 1996; Van der Meijde et al. 2003), which could provide insight into the deep Earth's volatile budget (Thompson, 1992).

⋆ E-mail: lijiaqi9@msu.edu

Although deep-focus earthquakes and cold temperatures in the subducting slab are associated, the mechanism for deep-focus earthquakes is still unclear. Interaction between the 410-km discontinuity and the subducting slab could reveal this critical question. Specifically, the 410-km discontinuity topography inside the subducting slab could be used to infer the existence of a metastable olivine wedge, a candidate to account for deepfocus earthquakes (Green Ii & Burnley 1989; Kirby et al. 1991).

To detect and further constrain the discontinuity, secondary seismic phases generated at the interface could be good candidates. The related methods can generally be classified into two categories: one is to use the reflected waves off the interfaces (e.g., Flanagan & Shearer (1998, 1999); Gu & Dziewonski (2002); Schmerr & Garnero (2007); Houser et al. (2008); Lawrence & Shearer (2008); Ritsema et al. (2009b); Wang et al. (2017); Li et al. (2019b); Tian et al. (2020); Wei et al. (2020)); and the other is to use the converted wave upon transmissions at the discontinuities (e.g., Vinnik (1977); Collier & Helffrich (1997); Thirot et al. (1998); Chevrot et al. (1999); Niu et al. (2005); Ritsema et al. (2009a)). Although these secondary phases could provide direct constraints on the discontinuities, stacking over hundreds of traces is usually necessary to enhance the visibility of these minor phases.

An alternative approach is to use the regional (10^o - 30^o) multipathing seismic body waves that bottom near the interface. Unlike the phase conversions and reflections which are too weak to observe on an individual seismogram, these multipathing waves (triplications) are clearly recorded at a single station. Moreover, distinct triplication branches with different move-out slopes can be observed in record sections of dense seismic arrays.

Since 1967, travel times of triplicated body-wave phases have been used to constrain the 1-D upper mantle structure (Johnson 1967). Later on, waveform matching, between observed and synthetic seismograms has been used to find the best fitting 1-D wave speed profile (e.g., Grand & Helmberger (1984); Tajima & Grand (1995); Brudzinski & Chen (2000); Wang et al. (2009)). However, due to the complexity of the waveforms, most of these studies rely on a trial-and-error approach.

Some efforts towards the automatic inversion have been made by applying the conjugate gradient method (Gao et al. 2006). However, for this gradient-based method, finding an appropriate initial model to avoid falling into the local minima is challenging, especially for the complex triplication data. Moreover, the inverted model's quantitative error estimation is hard to derive (Shearer 2000), and possible tradeoffs between model parameters need systematic considerations.

With the rapid development of full-waveform inversion (FWI), triplicated waveforms are

also recently incorporated into the 3-D FWI framework (Tao et al. 2018). Nevertheless, the shortest period for regional FWI is $\sim$ 8s due to the vast computational cost for a higher frequency, which limits the resolution. Also, the currently available data may still not be adequate to constrain 3-D models well. For both reasons, 1-D simulation and inversion, using high frequency data (up to $\sim$ 1 Hz) and few parameters, is still a useful approach to reveal the seismic structure in certain regions, especially near the turning points of seismic waves.

In this paper, we first introduce the concept of triplications. Then, we systematically analyze the tradeoff between model parameters, through forward modeling and waveform inversion. We also illustrate the necessity of using array normalized amplitude. Finally, with the non-gradient-based inversion package we developed, we show a real data example for the 1-D wave speed profile below the Tatar Strait of Russia.

2 MULTIPATHING TRIPLICATED BODY WAVES

Triplications originate when seismic body waves encounter regions where wave speed increases sharply with depth (e.g., the Moho, the 410-km (660-km) discontinuity, and the slab upper surface). Near such discontinuities or steep gradients, body waves (both P and S waves) will propagate in different paths. Fig. 1a shows an example of the raypath geometry and corresponding synthetic seismograms of P-wave triplications caused by the 410-km discontinuity. To clearly show the triplicated phases, in this section we use the WKBJ code of Chapman (1978), which enables us to separately calculate each of the three branches. The synthetics are computed using the seismic reference model IASP91 (Kennett & Engdahl 1991), assuming an earthquake source at 114 km depth. The three branches consist of the direct branch (AB), the reflected branch (BC), and the refracted branch (CD), which are illustrated in Fig. 1b, 1c, and 1d, respectively. We use the source-receiver geometry shown in Fig. 1 for synthetic tests throughout this paper, although subsequent modelings use more realistic attenuation (t^* of 1 s) and a Gaussian source time function, instead of the stick diagram here. We should also note that here we haven't applied normalization to this synthetic case so that the amplitude variations between stations are kept. As shown in Fig. 1a, these triplicated phases provide dense samplings of the 410-km discontinuity. Since the raypaths of the different triplication branches deviate only slightly from each other in the shallow part, the relative travel times and amplitudes of triplications can be attributed primarily to the structure near the transition zone.

3 THE TRADEOFF BETWEEN MODEL PARAMETERS

3.1 The tradeoff between discontinuity depth and low wave speed above the 410-km discontinuity

The existence of a low wave speed zone above the 410-km discontinuity, indicative of partial melting, will provide evidence for the water content in the mantle transition zone (Bercovici & Karato 2003). Some researchers using converted or transmitted phases have observed the existence of the low wave speed zone above the 410-km discontinuity in some regions (Revenaugh & Sipkin 1994; Schmandt et al. 2011; Wei & Shearer 2017). Such anomaly has also been indicated from constraints of triplication data (e.g., (Song et al. 2004; Li et al. 2019a; Han et al. 2020)).

Here we perform an ideal synthetic case without noise, to test the sensitivity of triplications to the low wave speed zone above the interface. For the model setup, we keep the wave speed at 360 km the same as the IASP91 model, and decrease the wave speed at 410 km by 0.1 km/s, to represent a low wave speed gradient within 50 km above the 410-km discontinuity (Fig. 2a).

We calculated both the travel time curves and waveforms (amplitude normalized by each trace) for this case. We should note that for this modeling here and all the others in subsequent parts, we use the QSEIS program (Wang 1999) to calculate the full wavefield, instead of specified phases by the WKBJ program in Fig. 1. As shown in the travel time curves, the low wave speed zone above the discontinuity mainly affects the extension of the OB branch (the red line in Fig. 2b). Specifically, in this case, the direct waves (OB branch) terminates at a larger epicentral distance, thereby increasing the OB branch's amplitude (the shaded grey area in Fig. 2c). This phenomenon has also been observed by previous researchers (e.g. Li et al. (2017, 2019a); Han et al. (2020)), and been used to detect the existence of the low wave speed zone.

However, other model candidates also have such equivalent behavior near cusp B. For example, we show a comparison between this model (the red line in Fig. 2a) with another equivalent model with a depressed interface but with a normal wave speed gradient (the blue line in Fig. 2a). The travel time curves (Fig. 2b) show that both of these two models will extend the OB branch to farther distance, but to different degrees. Specifically, the model with a low wave speed layer above the interface has a longer extension of the OB branch.

However, the waveforms of the OB branch, where the amplitude of it is large enough to observe, are quite similar for these two models (the shaded gray area in Fig. 2c and Fig. 2d),

indicating that this tradeoff does exist. We should note that the amplitude of the waveforms show some discrepancies with the travel time curves (e.g., Fig. 2b shows that the OB branch terminates at 21 ^{o}, indicating a much smaller amplitude of it than what we have seen in Fig. 2d). This inconsistency comes from two reasons. The first is the difference between the ray theory and the finite frequency effect. The waveform comparison, which takes the finite frequency effect into account, is more reliable and closer to the real situation. The other reason is from the normalization by each trace, which we will discuss in the next subsection.

This tradeoff has also been noticed by some researchers (e.g., Wang & Chen (2009); Song et al. (2004)), and they tried to rule out such model candidates. For example, Wang & Chen (2009) analyzed similar model pairs for the 660-km discontinuity, and denied the model with a depressed interface based on its different slope for the OC branch in the travel time curves. According to our test, even if there are some differences for the slope of the OC in the travel time curves (Fig. 2b), the differences in the corresponding waveforms for the OC branch are more subtle (e.g., less than a quarter of the wavelength). Another reason why the waveforms in our case look more identical is that we applied our waveform inversion code to search for this equivalent model (out of 15,000 models).

Song et al. (2004) also discussed these two types of models for the 410-km discontintuity by comparing the waveforms. The model with a depressed interface is ruled out due to its failure to generate the visible waveforms of the OB branch (Song et al. 2004). However, the proposed model in our case can generate a clear OB branch whose amplitude is equivalent to the model with a low wave speed zone above the interface. This discrepancy could partly come from the different earthquake sources we choose (different depths and focal mechanisms). Another possibility is that our synthetic model has an extra localized high wave speed anomaly below the interface. Assuming without this anomaly in the MTZ, the CD branch will be delayed. Thus, if viewed in the velocity seismograph (e.g., Song et al. (2004)), the negative pulses of the delayed CD branch will partly overlap with the OB branch and lower its amplitude.

We should note that this equivalent model we proposed might not be consistent with other constraints in certain regions (e.g., the receiver function results in Song et al. (2004)). However, theoretically, these two models are identical in our current settings. Therefore, triplication data alone cannot well constrain a low wave speed zone due to the tradeoff between the interface's depth and the wave speed gradient above it, especially when we normalize the amplitude by each trace.

3.2 Array normalization

In most of the previous triplication studies, people prefer to normalize the waveforms by each trace. Normalization is needed because of the uncertainties in the source magnitude, fault plane solution, attenuation, and station site effects, which make the absolute amplitudes more difficult to constrain. However, when using the normalized amplitude of each trace, information about the amplitude variations between stations is lost.

In this paper, we propose to use array normalization rather than trace normalization. In a record section, array normalization means that we normalize all traces relative to one particular reference station. Because all the records are from the same earthquake, the source magnitude's uncertainty won't affect the results after array normalization. Besides, within the narrow azimuthal range for the particular record section, the effect of uncertainty in the fault plane solution is also slight. When we invert for one discontinuity, the range of epicenter distance is only about within ten degrees. Therefore, we expect the attenuation near the discontinuity within this relatively smaller range should not change dramatically. Nevertheless, suppose we have observed stations with unusual amplitudes either due to attenuation or site effects, we could use trace normalization for these certain stations or reduce the weighting for them.

We first compare the trace normalization and array normalization for the two models shown before (Fig. 2a). In the array-normalized waveforms (Fig. 3a) where amplitude information between stations is kept, we do observe differences in amplitude between these two models (the shaded grey region in Fig. 3a). Specifically, the amplitude of the OB branch for the blue one is smaller than the red one, although still larger than the IASP91 model. Besides, the amplitude for the OD branch is also different. If we carefully examine the model with a depressed interface (Fig. 2a) within the depth range from 410 km to 470 km, we will find that although the absolute wave speed is larger than the IASP91 model, the wave speed gradient is smaller. It is the wave speed gradient that mostly controls the waveform amplitude. Therefore, the amplitude of the OD branch is reduced due to this low wave speed gradient.

When we apply the traditional trace normalization (Fig. 3b), there are no obvious differences between the waveforms for these two model types, because the amplitudes of both the OD and OB branch are magnified. In other words, the larger amplitude of the OB branch comes from the magnification of the trace normalization due to the smaller amplitude of the OD branch. Therefore, amplitude information between stations in the record section is critical to reducing the non-uniqueness of the models.

Here, we show another comparison between trace normalization and array normalization

to illustrate the necessity of applying array normalization. As shown in Fig. 4c and Fig. 4d, the black model shown is the IASP91 model, and the red model is a designed model with a -0.4 km/s low wave speed layer only in the shallow part (< 150 km). As shown in Fig. 4a, the array-normalized seismography demonstrates that the different structures in the shallow part will cause an overall time delay (of $\sim$ 3 s) and affect the amplitude of the direct wave (AO). In comparison, the amplitudes of the later phases (CO) remain basically unchanged. However, for trace normalization, because the amplitude for the direct wave (AO) is always the largest within the epicentral distance range before 15^o, the amplitude of the direct wave is always unity after normalization (Fig. 4b). Therefore, the amplitude of the later phases (CO), whose amplitude is originally unchanged, seems to have a smaller amplitude after the trace normalization. We should note that the later phases correspond to the reflected wave at the 410-km discontinuity and the transmitted wave below it. In this way, the deeper structure is likely to be incorrectly adjusted (Fig. 4d).

As such, besides losing the waveform information between stations (increasing tradeoff), trace normalization will also lead to the misunderstanding of the corresponding structure for the mismatch in the waveforms, which further affects the inversion result. Therefore, we recommend using this array-normalization approach.

3.3 Synthetic inversion test

Using array normalization, the tradeoff between the interface's depth and the wave speed gradient above it can be minimized. Here, we will perform a synthetic inversion test to show to what extent this tradeoff will be reduced and how much of it still remains.

To obtain quantitative error bounds and avoid the risk of falling into the local minima faced by the gradient-based inversion method, we adopt the niche genetic algorithm (Koper et al. 1999; Li et al. 2012) into the inversion framework of triplicated waveforms. Niche genetic algorithm (NGA) is a non-gradient-based inversion scheme that searches the model space through massive forward modeling. NGA is independent of the initial model. Only the search range of the model space is given as a priori. Moreover, because NGA involves numerous samplings in the model space, it can finally output a series of acceptable model sets. The mean and variance of these acceptable models can help estimate the uncertainty of the final model.

We designed a P-wave synthetic test and array normalization is applied. In this test, we set the IASP91 model as the "ground truth", and let its corresponding synthetic displacement waveforms be inverted. We set the maximum epicentral distance to be 21 ^{o} because within this

range the OB branch is large enough to observe. In the inversion model setup, considering the ray paths' penetration depths, we only invert the structure from 210 km to 560 km depth. Within this depth range, totally we set nine parameters to invert. Specifically, three parameters are on the '410-km' discontinuity to capture the sharp gradient: two of them are immediately on the discontinuity to represent the wave speed jump, another one is its depth variation. In addition, three parameters are set with an interval of $\sim$ 40 km, above and below the interface, respectively. We should note that for these six anchor points which reflect more gradual wave speed change away from the discontinuity, we only invert the wave speed at these points. Between two adjacent points, the wave speed is linearly interpolated. Beyond this depth range, the wave speed is fixed to the value in the IASP91 model. The P wave speed at each anchor point is allowed to vary between plus and minus 0.3 km/s, and the position of the discontinuity varies within plus or minus 20 km, based on the IASP91 model (Fig. 5a). The P wave speed is the only unknown parameter for each anchor point, and the Poisson's ratio and density are the same as those in the IASP91 model. The effect of attenuation for P wave is considered by applying a constant t* value of 1s.

As for the misfit window, we choose a continuous one from 32 s to 52 s (reduced time) which contains the entire triplicated P wave train, for this ideal case without noise. Prior to the calculation of the misfit, we first cross-correlate the theoretical and observed waveform for the ith station to obtain the time difference Δt_i. After shifting the synthetic trace by Δt_i, we calculate the L2 norm of the differences between the observed and aligned synthetic waveform in the time domain as the misfit function χ_{L2}:

$$\chi_{L2} = \sum_{i=1}^{N} \int_{t_1}^{t_2} |\mathbf{d}(\mathbf{x}_i, t) - \mathbf{u}(\mathbf{x}_i, t + \Delta t_i)|^2 dt, \tag{1}$$

Where $\mathbf{d}(\mathbf{x}_i, t)$ is the displacement data recorded by the ith station, $\mathbf{u}(\mathbf{x}_i, t + \Delta t_i)$ is the synthetic data for the ith station after a time shift of Δt_i. t_1 and t_1 are the start and end time for the misfit window, respectively. N is the total number of stations used in the inversion.

This method converges very quickly. After the first 20 generations (100 simulations per generation), the residuals significantly reduce. And after 80 generations, the residuals are stable (Fig. 5c). From the 100 models in the last generation, we further define the acceptable model limits by a 10% increase in the misfit than the best model or by visually comparing the data and synthetics when the misfit does not readily detect the mismatch.

Finally, we have got three typical acceptable model groups (Fig. 5a). The first model groups converge to the ground truth model, verifying the effectiveness of our triplication

inversion package. The other two model groups (group 2 and group 3) are just the exact model pairs we discussed before.

We further use the averaged value of these two groups of models to calculate their corresponding displacement waveforms. Waveforms between these two groups are almost identical, and both of them are also quite similar to the IASP91 model's waveforms (Fig. 5b).

This synthetic test shows that even if the array normalization is applied, this tradeoff between the interface's depth and the wave speed gradient above it can not be eliminated. The reason is that a depressed interface truly has a similar impart on the amplitude of the OB branch compared with a low wave speed gradient above the interface (Fig. 3a). And some differences between these two models in the waveforms are less obvious compared with the travel time curves (Fig. 3b) due to the finite frequency effect.

Thus, this tradeoff between the interface's depth and the wave speed gradient above it does exist. Nevertheless, for a given frequency band, we could estimate the depth uncertainty due to this tradeoff. One possible approach is to compare waveforms between possible models to find the acceptable minimum and maximum depth limits for the interface. These depth limits can be quickly found using this automatic inversion program. For this case, given this frequency band and misfit tolerance, the tradeoff from the wave speed above the discontinuity will lead to a $\sim$ 10 km uncertainty of the depth estimation.

3.4 No tradeoff between discontinuity depth and wave speed in the MTZ

Fast P-wave speed in the MTZ has been observed in a particular region beneath the Tonga backarc (Brudzinski & Chen 2000). In the western Pacific subduction zone, tomography results (Huang & Zhao 2006; Chen & Pei 2010) indicate a 'flat slab' in the MTZ, which also increases the wave speed in the mantle transition zone.

We first test the triplication's sensitivity to this higher wave speed in the MTZ. Here we calculated the travel time curves when the wave speed below the 410-km discontinuity is increased by 0.1 km/s (Fig. 6b) relative to the IASP91 model, using the Taup toolkit (Crotwell et al. 1999). Travel time curves show that the wave speed in the MTZ significantly impacts the CD branch's travel time (Fig. 6d). In other words, the increase of the wave speed below the discontinuity will make the transmitted waves (CD) travel faster. Crossover point (O) marks the intersection of the AB and CD branch, where the waveform amplitude reaches its maximum. Therefore it is one of the most obvious signatures of this triplication. In this case, the earlier arrivals of the CD branch will cause the crossover point (O) to appear at a smaller epicentral distance.

Similar behavior of the travel time curves occurs when the depth of the interface is shallower. And near the subducting slab, the 410-km discontinuity can be elevated due to the positive Clapeyron slope (e.g., Bina & Helffrich (1994); Flanagan & Shearer (1998)). Assuming a situation where the 410-km discontinuity has a 30-km uplift (Fig. 6a), the CD branch arrives earlier, and consequently, the crossover point (O) occurs at a smaller distance (Fig. 6c). This is because, in this situation, this elevated interface is equivalent to a high wave speed anomaly between 380 km and 410 km.

One difference between these two situations is that when the 410-km discontinuity is uplifted, the earlier arrival of the CD branch can be seen from its beginning (cusp C in Fig. 6c and Fig. 6e). While for another case where a high wave speed exits in the MTZ, the advance of the CD branch is not obvious until the epicentral distance is larger than the crossover distance (O in Fig. 6d and Fig. 6f). Therefore, it is critical to have stations with smaller epicentral distance (before the crossover point).

However, near the subduction zone, stations near the epicenter are often scarce compared to more distant stations. This fact sometimes makes it difficult to distinguish between the two situations. Nevertheless, careful waveform analysis could provide more clues. Specifically, in the case of a more considerable wave speed jump, the amplitude near cusp B remains unchanged (the shaded grey area in Fig. 6f). On the other hand, with an uplifted 410-km discontinuity, the amplitude near cusp B is smaller (the shaded grey area in Fig. 6e).

Therefore, with waveform information, even if the travel time differences between the OB and OD branches are almost identical for these two situations (Fig. 6c and 6d), we can make an unambiguous distinction between them (Fig. 6e and 6f).

4 APPLICATION TO THE KURIL SUBDUCTION ZONE

We focus on an intermediate depth (114 km) event that occurred in the Kuril subduction zone on October 10, 2009, with Mw $\sim$ 5.9 (Fig. 7a). This study's triplication waveforms are from a subset of the broadband CEArray (Zheng et al. 2010) in northeast China. We choose the P-wave data to achieve a better resolution because the P wave is typically observed at a higher frequency than the S wave due to its smaller attenuation. Therefore, even though the wave speed of the P wave is faster than that of the S wave, the P wave still has a smaller Fresnel zone. After removing the instrument response, we have applied a first-order, zero-phase shift Butterworth filter with frequency band 0.05-1 Hz to the data. We choose this relatively broad frequency band to avoid distortion of the data. Because the azimuth range of this selected

sublinear array is relatively narrow (2^o), one model should explain all the waveforms in the record section.

Given the fact that with this triplication data alone we cannot exclusively judge the presence of a low wave speed zone above the 410-km discontinuity, therefore we fix the gradient above the interface no less than the value in the IASP91 model. As such, we can focus more on the first order location of the discontinuity. But we should know that at this frequency band, the tradeoff from the low wave speed gradient above will introduce a depth uncertainty of $\sim$ 10 km (Fig. 5a).

Waveforms in this case are more complex than those in the synthetic test (Fig. 5b). Specifically, there are two triplications in this record section (Fig. 7b), indicating more than one discontinuity. Accordingly, we set two interfaces in the inversion setup and finally obtain such acceptable models (the shaded red region in Fig. 7d). We choose one of them to generate the synthetics and the waveforms generally show good agreement for both the relative timing and amplitudes in each trace and the amplitude variations between stations (Fig. 7b).

The inversion results show that the first discontinuity is located at 400 km depth (Fig. 7d). Based on all the acceptable models, the depth uncertainty is estimated to be 5 km. Besides, there is another discontinuity at 480$\pm$10 km depth. We should note that the uncertainty here is from the data itself. If we consider the tradeoff between model parameters, another 10-km uncertainty should be taken into account.

5 DISCUSSION

5.1 Frequency dependent resolution for discontinuity sharpness

In the inversion, we set all the discontinuities as sharp interfaces. This is because given the duration of the source time function of $\sim$ 2 s, we cannot discern a model with a sharp jump from the model with a gradual interface. In this subsection, we want to discuss the smallest discernible thickness of the discontinuity, at different frequency bands, through forward modeling.

We take the 410-km discontinuity as an example, We set its location in the IASP91 model as the midpoint and vary the thickness between 0 km and 40 km (Fig. 8a). Travel time curves show that the increase of the discontinuity thickness has the strongest impact on the BC branch. Specifically, the thickened discontinuity will considerably "shrink" the reflected wave branch BC, although it has little effect on the arrivals of the direct wave branch AB and the transmitted wave branch CD (Fig. 8b).

However, the corresponding waveforms seem to indicate quite different conclusions from the travel time curves. Specifically, no noticeable difference of the BC branch can be seen even the thickness of the discontinuity increases to 40 km (Fig. 8c). This discrepancy is because the travel time curve is calculated based on ray theory. However, this waveform modeling period is 3 s, where wavefront healing occurs due to the finite frequency effect.

To further study this frequency dependent feature, we performed forward modelings for the model with a discontinuity thickness of 40 km, with different duration for the source time function of 3 s, 2 s, and 1 s, respectively (Fig. 8c, 8d, 8e). Results show that as the frequency increases, the waveform differences between this gradual model and the sharp IASP91 model become more apparent (especially for the pre-critical reflections at a smaller epicentral distance). Moreover, when the waveform period is greater than 3 s, it is impossible to distinguish the discontinuity between a sharp interface and a gradual one with 40 km thickness, even without adding noise. A similar frequency dependent feature has also been observed in previous triplication studies (Melbourne & Helmberger 1998; Zhang et al. 2019).

According to these synthetic tests, given the duration of the source time function $\sim$ 2 s, we cannot discern a model with a sharp jump across the 410-km discontinuity from the model with a gradual interface with a 20-km width. Therefore, in the inversion, we set the discontinuity as a sharp interface. Nevertheless, the inverted interface's depth should coincide with the center of the actual (perhaps wider) interface.

To provide more constraints on the discontinuity's sharpness, we could filter the broadband record into short-period data, but at the cost of losing other useful information. An alternative way is to choose smaller events with a shorter source time function. However, there always exists a contradiction between the smaller events and the lower SNR. Nevertheless, combining triplication data with converted or underside reflected phases could better constrain the discontinuity's sharpness.

5.2 Depth of the discontinuities

Even though the appearance of two triplications suggests the existence of two interfaces, we still designed forward modeling tests with only one discontinuity, to confirm the validity of two discontinuities in the model. Results show that the model without the slab upper surface (the blue one in Fig. 9b) cannot fit the longer duration of the signals near $\sim 20^o$ (Fig. 9a).

The turning points, the most sensitive regions of the triplicated ray paths, are below the Tatar Strait of Russia. Our derived first interface at 410$\pm$5 km is consistent with the overall 0-10 km uplift of the 410-km discontinuity in this region observed with ScS reverberations

(Wang et al. 2017). Furthermore, our result is of higher resolution due to the smaller Fresnel zone for the P wave at a higher frequency ($\sim$ 0.5 Hz).

As for the deeper discontinuity located at 480$\pm$10 km, it is partly consistent with the +1% wave speed contour of the regional tomography results (Tao et al. 2018). Therefore, we propose this second interface to be the slab upper surface. It is not surprising that our derived interface is shallower than the Slab2.0 model (Hayes et al. 2018). First, the speculated slab upper surface from the Slab2.0 model is based on an assumed thickness of the subducting oceanic lithosphere and precise locations of the seismicities. Second, the Slab2.0 model (Hayes et al. 2018) doesn't have enough data in our research region (e.g., the black line terminated at 8 ^{o} in Fig. 7c).

Wang et al. (2014) and Tao et al. (2017), through waveform modeling, have shown that some 2-D and 3-D slab structures near the turning points can influence triplicated waveforms. To avoid this interference, we specifically choose the event whose ray paths are roughly parallel to the slab's depth contour. As such, in this particular direction, the slab seems to be flat near the turning points (Fig. 7c) and it can still satisfy the 1-D inversion assumption. Therefore, the inverted depth of 480$\pm$10 km, derived from 1-D inversion, is reliable.

As such, the upper slab surface is located $\sim$ 70 km below the 410-km discontinuity (Fig. 7c). The cooling effect from this relatively distant slab is weak, therefore no observable uplift of the 410-km discontinuity is observed.

5.3 Wave speed jumps across the discontinuities

As for the inverted wave speed, we should note that there could be a baseline shift in our inverted models because we cannot constrain the absolute wave speed value due to the cross-correlation alignment we used. Therefore, instead of the absolute wave speed, we pay more attention to the wave speed jump across the discontinuity, which is much better constrained.

From the synthetic test in Fig. 5a, we notice that the inverted models might have some small scale wave speed deviations from the ground truth model below the interface. However, these deviations vanish when it is farther away from the interface. These artifacts are probably due to the inversion parameterization and the frequency dependent resolution issue. Therefore, it is not appropriate to directly use the points immediately above and below the interface to calculate the wave speed jump. Instead, we choose the points 20 km above and below the inverted interface to measure the wave speed jump for both the inverted model sets and the IASP91 model. In this way, the wave speed jump across the 410-km discontinuity and the slab upper surface is $\sim$ 7.5% and $\sim$ 7%, respectively.

435 This method of measurement over a distance of 40 km can minimize some artifacts. How-
436 ever, the wave speed jump of $\sim$ 7% is $\sim$ 2% larger than the value of 5.2% for the 410-km
437 discontinuity in the IASP91 model, and $\sim$ 5%-6% larger than the 1%-2% slab contours in the
438 regional tomography results (Tao et al. 2018). This extra wave speed jump could be partly
439 due to the failure of the 1-D assumption in the source region. This is because, near the source
440 site, the high wave speed slab is roughly parallel to the ray paths. Although using relative time
441 and amplitudes of the triplicated phases could eliminate the effect of lateral heterogeneities
442 at shallow depth, this accumulated effect of the source-site anomalies along the ray paths
443 cannot be neglected (Li et al. 2016). Therefore, this extra wave speed jump may be partly
444 overestimated due to the failure of the 1-D assumption near the source site.

445 For the 410-km discontinuity, if this extra $\sim$ 2% wave speed jump is not totally overes-
446 timated, it could reflect the existence of a localized high wave speed anomaly just below the
447 interface. Consistently, we found that in the regional tomography results (Tao et al. 2018),
448 there is a localized +1% wave speed contour around the 410-km discontinuity near epicentral
449 distance $\sim 9^o$ in Fig. 7c. The existence of this localized high wave speed feature to some extent
450 confirms our inverted larger wave speed jump.

451 For the slab upper surface, because we are using higher frequency data ($\sim$ 2 s), the interface
452 should be sharper in our results compared with the regional tomography results based on lower
453 frequency data ($\sim$ 8 s). However, our derived wave speed jump of $\sim$ 7% is significantly larger
454 than the 1%-2% slab contours in the regional tomography results (Tao et al. 2018). We should
455 note that our derived apparently larger wave speed jump doesn't contradict with the much
456 smaller value from tomography results (Fukao et al. 2001; Tao et al. 2018). This is because
457 there is a low wave speed anomaly in the inverted model, and this low wave speed anomaly
458 above the upper slab surface partly contributes to this huge apparent wave speed contrast.

459 To confirm the validity of this low wave speed zone and examine whether or not it is an
460 artifact to compensate for the larger wave speed jump across the 410-km discontinuity, we
461 conducted forward modeling test using a model in which the low wave speed zone is replaced
462 by a uniform layer with the averaged wave speed (Fig. 9c). Results show that the model with
463 the averaged wave speed in the low wave speed zone can only account for the relative timings
464 of the triplicated phases, but the amplitudes of the first phase at epicentral distances of $\sim$
465 18^o are $\sim$ 10-20% larger than the records (the shaded grey area in Fig. 9d). Thus both the
466 larger wave speed jump across the 410-km discontinuity and the low wave speed zone above
467 the slab upper surface are necessary to fit the triplicated waveforms.

468 Consistently, a low wave speed anomaly above the slab can also be seen in the tomography

model of Tao et al. (2018), at $\sim 7^o$ epicentral distance, although of smaller amplitude. Based on both observations, we propose that this low wave speed zone above the slab upper surface does exist. However, whether it is a thermal anomaly or caused by the dehydration of the subducting slab, needs more evidence (e.g., wave speed of the S wave).

We should also note that we can only qualitatively prove the existence of this low wave speed anomaly. To further constrain its precise wave speed, 2-D or 3-D corrections are needed which take the source-site influence into account. In addition, more events and stations are needed to obtain a 3-D mapping of the discontinuities here.

6 CONCLUSIONS

Triplicated body waves have rich information and can effectively sample the structure near the transition zone. Although 1-D triplication inversion is a useful and efficient approach, the tradeoff between model parameters should be carefully considered.

We have systematically analyzed the tradeoff between the depth of the discontinuity and the low wave speed gradient above it, through forward modeling and waveform inversion. We also illustrate the necessity of using array normalized amplitude.

Finally, we inverted the 1-D structure below the Tatar Strait of Russia. We have observed triplications for both the 410-km discontinuity and the slab upper surface, and simultaneously derived seismic structures for these two interfaces. The upper surface of the slab is located at 480±10 km, which is consistent with the location of the 1% wave speed contour of the regional tomography results (Tao et al. 2018), but with a larger amplitude. This significant wave speed jump of $\sim 7\%$ is contributed by both the differences across the slab upper surface and a low wave speed anomaly above the subducting slab. The 410-km discontinuity is located at 410±5 km, indicating little thermal influence from the distant subducting slab located $\sim$ 70 km below it.

ACKNOWLEDGMENTS

Seismic records used in this study came from the CEArray, and we thank the team members for their deployments. We thank Chunquan Yu for helping with the 2-D simulation and Shawn S. Wei, Mingda Lv, Xiaobo He, Megan Flanagan, Ziyi Xi, Guoliang Li, and Zhigang Peng for valuable discussion. We acknowledge the course "English Composition for Geophysical Research" by Li Zhao of Peking University for help in improving this manuscript. We thank the IRIS Data Management Center for the access to waveforms used in the focal depth inversion.

We thank the Institute for Cyber-Enabled Research (ICER) at Michigan State University, the Extreme Science and Engineering Discovery Environment (XSEDE supported by NSF grant ACI-1053575), and the High-performance Computing Platform of Peking University for providing the high-performance computing resources. The map-view figure is produced using the GMT software of Wessel & Smith (1998). This research was supported by NSF grant 1802247 and the startup fund of Min Chen at Michigan State University.

REFERENCES

Bercovici, D. & Karato, S.-i., 2003. Whole-mantle convection and the transition-zone water filter, *Nature*, **425**(6953), 39–44.

Bina, C. R. & Helffrich, G., 1994. Phase transition clapeyron slopes and transition zone seismic discontinuity topography, *Journal of Geophysical Research: Solid Earth*, **99**(B8), 15853–15860.

Brudzinski, M. R. & Chen, W.-P., 2000. Variations in p wave speeds and outboard earthquakes: evidence for a petrologic anomaly in the mantle transition zone, *Journal of Geophysical Research: Solid Earth*, **105**(B9), 21661–21682.

Chapman, C. H., 1978. A new method for computing synthetic seismograms, *Geophysical Journal International*, **54**(3), 481–518.

Chen, Y. J. & Pei, S., 2010. Tomographic structure of east asia: Ii. stagnant slab above 660 km discontinuity and its geodynamic implications, *Earthquake Science*, **23**(6), 613–626.

Chevrot, S., Vinnik, L., & Montagner, J.-P., 1999. Global-scale analysis of the mantle pds phases, *Journal of Geophysical Research: Solid Earth*, **104**(B9), 20203–20219.

Collier, J. D. & Helffrich, G. R., 1997. Topography of the "410" and "660" km seismic discontinuities in the izu-bonin subduction zone, *Geophysical research letters*, **24**(12), 1535–1538.

Crotwell, H. P., Owens, T. J., & Ritsema, J., 1999. The taup toolkit: Flexible seismic travel-time and ray-path utilities, *Seismological Research Letters*, **70**(2), 154–160.

Flanagan, M. P. & Shearer, P. M., 1998. Global mapping of topography on transition zone velocity discontinuities by stacking ss precursors, *Journal of Geophysical Research: Solid Earth*, **103**(B2), 2673–2692.

Flanagan, M. P. & Shearer, P. M., 1999. A map of topography on the 410-km discontinuity from pp precursors, *Geophysical research letters*, **26**(5), 549–552.

Fukao, Y., Widiyantoro, S., & Obayashi, M., 2001. Stagnant slabs in the upper and lower mantle transition region, *Reviews of Geophysics*, **39**(3), 291–323.

Gao, W., Matzel, E., & Grand, S. P., 2006. Upper mantle seismic structure beneath eastern mexico determined from p and s waveform inversion and its implications, *Journal of Geophysical Research: Solid Earth*, **111**(B8).

Grand, S. P. & Helmberger, D. V., 1984. Upper mantle shear structure of north america, *Geophysical Journal International*, **76**(2), 399–438.

Green Ii, H. & Burnley, P., 1989. A new self-organizing mechanism for deep-focus earthquakes, *Nature*, **341**(6244), 733–737.

Gu, Y. J. & Dziewonski, A. M., 2002. Global variability of transition zone thickness, *Journal of Geophysical Research: Solid Earth*, **107**(B7), ESE–2.

Han, G., Li, J., Guo, G., Mooney, W. D., Karato, S.-i., & Yuen, D. A., 2020. Pervasive low-velocity layer atop the 410-km discontinuity beneath the northwest pacific subduction zone: Implications for rheology and geodynamics, *Earth and Planetary Science Letters*, p. 116642.

Hayes, G. P., Moore, G. L., Portner, D. E., Hearne, M., Flamme, H., Furtney, M., & Smoczyk, G. M., 2018. Slab2, a comprehensive subduction zone geometry model, *Science*, **362**(6410), 58–61.

Helffrich, G. R. & Wood, B. J., 1996. 410 km discontinuity sharpness and the form of the olivine α-β phase diagram: resolution of apparent seismic contradictions, *Geophysical Journal International*, **126**(2), F7–F12.

Houser, C., Masters, G., Flanagan, M., & Shearer, P., 2008. Determination and analysis of long-wavelength transition zone structure using ss precursors, *Geophysical Journal International*, **174**(1), 178–194.

Huang, J. & Zhao, D., 2006. High-resolution mantle tomography of china and surrounding regions, *Journal of Geophysical Research: Solid Earth*, **111**(B9).

Johnson, L. R., 1967. Array measurements of p velocities in the upper mantle, *Journal of Geophysical Research*, **72**(24), 6309–6325.

Kawakatsu, H. & Watada, S., 2007. Seismic evidence for deep-water transportation in the mantle, *Science*, **316**(5830), 1468–1471.

Kennett, B. & Engdahl, E., 1991. Traveltimes for global earthquake location and phase identification, *Geophysical Journal International*, **105**(2), 429–465.

Kirby, S. H., Durham, W. B., & Stern, L. A., 1991. Mantle phase changes and deep-earthquake faulting in subducting lithosphere, *Science*, **252**(5003), 216–225.

Koper, K. D., Wysession, M. E., & Wiens, D. A., 1999. Multimodal function optimization with a niching genetic algorithm: A seismological example, *Bulletin of the Seismological Society of America*, **89**(4), 978–988.

Lawrence, J. F. & Shearer, P. M., 2008. Imaging mantle transition zone thickness with sds-ss finite-frequency sensitivity kernels, *Geophysical Journal International*, **174**(1), 143–158.

Li, G., Bai, L., Zhou, Y., Wang, X., & Cui, Q., 2017. Velocity structure of the mantle transition zone beneath the southeastern margin of the tibetan plateau, *Tectonophysics*, **721**, 349–360.

Li, G., Li, Y. E., Zhang, H., Bai, L., Ding, L., Li, W., Cui, Q., & Zhou, Y., 2019a. Detection of a thick and weak low-velocity layer atop the mantle transition zone beneath the northeastern south china sea from triplicated p-wave waveform modeling, *Bulletin of the Seismological Society of America*,

109(4), 1181–1193.

Li, J., Wang, S., C. C., & Ning, J., 2016. A computational scheme for quantitatively removing the effects of lateral velocity variation on 1-d triplicated wave velocity inversion, *Acta Scientiarum Naturalium Universitatis Pekinensis*, **52**(3), 420–426.

Li, L., Chen, Y.-W., Zheng, Y., Hu, H., & Wu, J., 2019b. Seismic evidence for plume-slab interaction by high-resolution imaging of the 410-km discontinuity under tonga, *Geophysical Research Letters*, **46**(23), 13687–13694.

Li, S.-H., Wang, Y.-B., Liang, Z.-B., He, S.-L., & Wen-Hao, Z., 2012. Crustal structure in southeastern gansu from regional seismic waveform inversion, *Chinese Journal of Geophysics*, **55**(2), 206–218.

Melbourne, T. & Helmberger, D., 1998. Fine structure of the 410-km discontinuity, *Journal of Geophysical Research: Solid Earth*, **103**(B5), 10091–10102.

Niu, F., Levander, A., Ham, S., & Obayashi, M., 2005. Mapping the subducting pacific slab beneath southwest japan with hi-net receiver functions, *Earth and Planetary Science Letters*, **239**(1-2), 9–17.

Revenaugh, J. & Sipkin, S., 1994. Seismic evidence for silicate melt atop the 410-km mantle discontinuity, *Nature*, **369**(6480), 474–476.

Ringwood, A. E., 1975. Composition and petrology of the earth's mantle, *MacGraw-Hill*, **618**.

Ritsema, J., Cupillard, P., Tauzin, B., Xu, W., Stixrude, L., & Lithgow-Bertelloni, C., 2009a. Joint mineral physics and seismic wave traveltime analysis of upper mantle temperature, *Geology*, **37**(4), 363–366.

Ritsema, J., Xu, W., Stixrude, L., & Lithgow-Bertelloni, C., 2009b. Estimates of the transition zone temperature in a mechanically mixed upper mantle, *Earth and Planetary Science Letters*, **277**(1-2), 244–252.

Schmandt, B., Dueker, K., Hansen, S., Jasbinsek, J. J., & Zhang, Z., 2011. A sporadic low-velocity layer atop the western us mantle transition zone and short-wavelength variations in transition zone discontinuities, *Geochemistry, Geophysics, Geosystems*, **12**(8).

Schmerr, N. & Garnero, E. J., 2007. Upper mantle discontinuity topography from thermal and chemical heterogeneity, *Science*, **318**(5850), 623–626.

Shearer, P. M., 2000. Upper mantle seismic discontinuities, *GEOPHYSICAL MONOGRAPH-AMERICAN GEOPHYSICAL UNION*, **117**, 115–132.

Song, T.-R. A., Helmberger, D. V., & Grand, S. P., 2004. Low-velocity zone atop the 410-km seismic discontinuity in the northwestern united states, *Nature*, **427**(6974), 530–533.

Tajima, F. & Grand, S. P., 1995. Evidence of high velocity anomalies in the transition zone associated with southern kurile subduction zone, *Geophysical research letters*, **22**(23), 3139–3142.

Tao, K., Grand, S. P., & Niu, F., 2017. Full-waveform inversion of triplicated data using a normalized-correlation-coefficient-based misfit function, *Geophysical Journal International*, **210**(3), 1517–1524.

Tao, K., Grand, S. P., & Niu, F., 2018. Seismic structure of the upper mantle beneath eastern asia from full waveform seismic tomography, *Geochemistry, Geophysics, Geosystems*, **19**(8), 2732–2763.

Thirot, J.-L., Montagner, J.-P., & Vinnik, L., 1998. Upper-mantle seismic discontinuities in a subduction zone (japan) investigated from p to s converted waves, *Physics of the earth and planetary interiors*, **108**(1), 61–80.

Tian, D., Lv, M., Wei, S. S., Dorfman, S. M., & Shearer, P. M., 2020. Global variations of earth's 520-and 560-km discontinuities, *Earth and Planetary Science Letters*, **552**, 116600.

Van der Meijde, M., Marone, F., Giardini, D., & Van der Lee, S., 2003. Seismic evidence for water deep in earth's upper mantle, *Science*, **300**(5625), 1556–1558.

Vinnik, L., 1977. Detection of waves converted from p to sv in the mantle, *Physics of the Earth and planetary interiors*, **15**(1), 39–45.

Wang, R., 1999. A simple orthonormalization method for stable and efficient computation of green's functions, *Bulletin of the Seismological Society of America*, **89**(3), 733–741.

Wang, T. & Chen, L., 2009. Distinct velocity variations around the base of the upper mantle beneath northeast asia, *Physics of the Earth and Planetary Interiors*, **172**(3-4), 241–256.

Wang, T., Revenaugh, J., & Song, X., 2014. Two-dimensional/three-dimensional waveform modeling of subducting slab and transition zone beneath northeast asia, *Journal of Geophysical Research: Solid Earth*, **119**(6), 4766–4786.

Wang, X., Li, J., & Chen, Q.-F., 2017. Topography of the 410 km and 660 km discontinuities beneath the japan sea and adjacent regions by analysis of multiple-scs waves, *Journal of Geophysical Research: Solid Earth*, **122**(2), 1264–1283.

Wang, Y., Wen, L., & Weidner, D., 2009. Array triplication data constraining seismic structure and composition in the mantle, *Surveys in geophysics*, **30**(4-5), 355–376.

Wei, S. S. & Shearer, P. M., 2017. A sporadic low-velocity layer atop the 410 km discontinuity beneath the pacific ocean, *Journal of Geophysical Research: Solid Earth*, **122**(7), 5144–5159.

Wei, S. S., Shearer, P. M., Lithgow-Bertelloni, C., Stixrude, L., & Tian, D., 2020. Oceanic plateau of the hawaiian mantle plume head subducted to the uppermost lower mantle, *Science*, **370**(6519), 983–987.

Wessel, P. & Smith, W. H., 1998. New, improved version of generic mapping tools released, *Eos, Transactions American Geophysical Union*, **79**(47), 579–579.

Zhang, M., Sun, D., Wang, Y., & Wu, Z., 2019. Fine structure of the 660-km discontinuity beneath southeastern china, *Geophysical Research Letters*, **46**(13), 7304–7314.

Zheng, X.-F., Yao, Z.-X., Liang, J.-H., & Zheng, J., 2010. The role played and opportunities provided by igp dmc of china national seismic network in wenchuan earthquake disaster relief and researches, *Bulletin of the Seismological Society of America*, **100**(5B), 2866–2872.

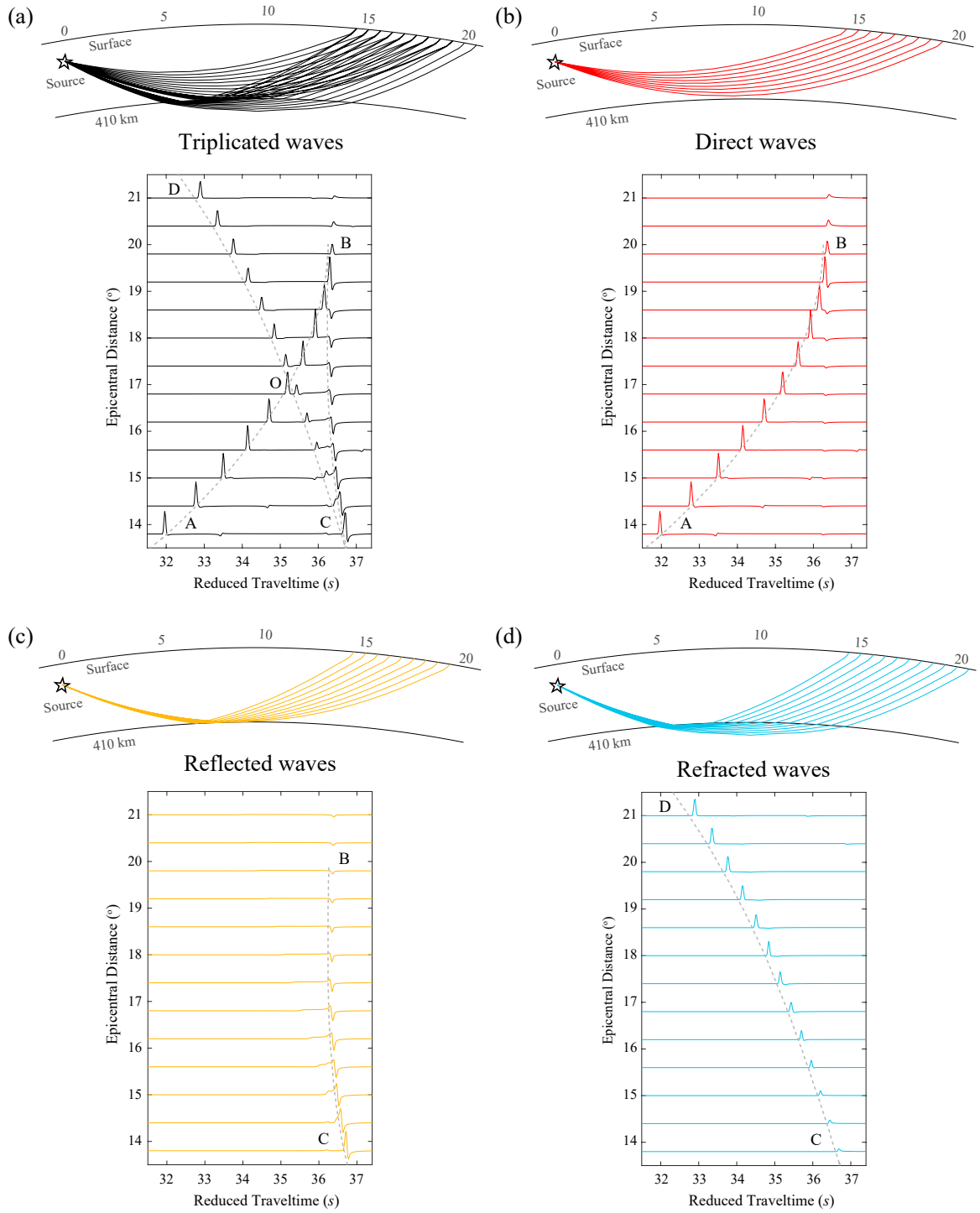

Figure 1. Ray paths and corresponding waveforms for triplications. (a) Ray paths and waveforms for all the triplicated P waves. In the upper panel, the black star is the earthquake source at 114km, and black lines show all the triplicated P wave ray paths. In the lower panel, the black waveforms are synthetics calculated by WKBJ (Chapman 1978) for the IASP91 model (Kennett & Engdahl 1991), and the dashed grey lines are the corresponding travel time curves calculated by Taup (Crotwell et al. 1999). AB, BC, and CD branches represent the direct waves, reflected waves, and refracted waves, respectively. The O point shows the crossover point of the AB and BC branch. A reducing slowness of 11.5 s/^{o} is used for the time plot. (b) Ray paths and waveforms for the direct waves AB with red color. (c) Ray paths and waveforms for the reflected waves BC with yellow color. (d) Ray paths and waveforms for the refracted waves CD with blue color.

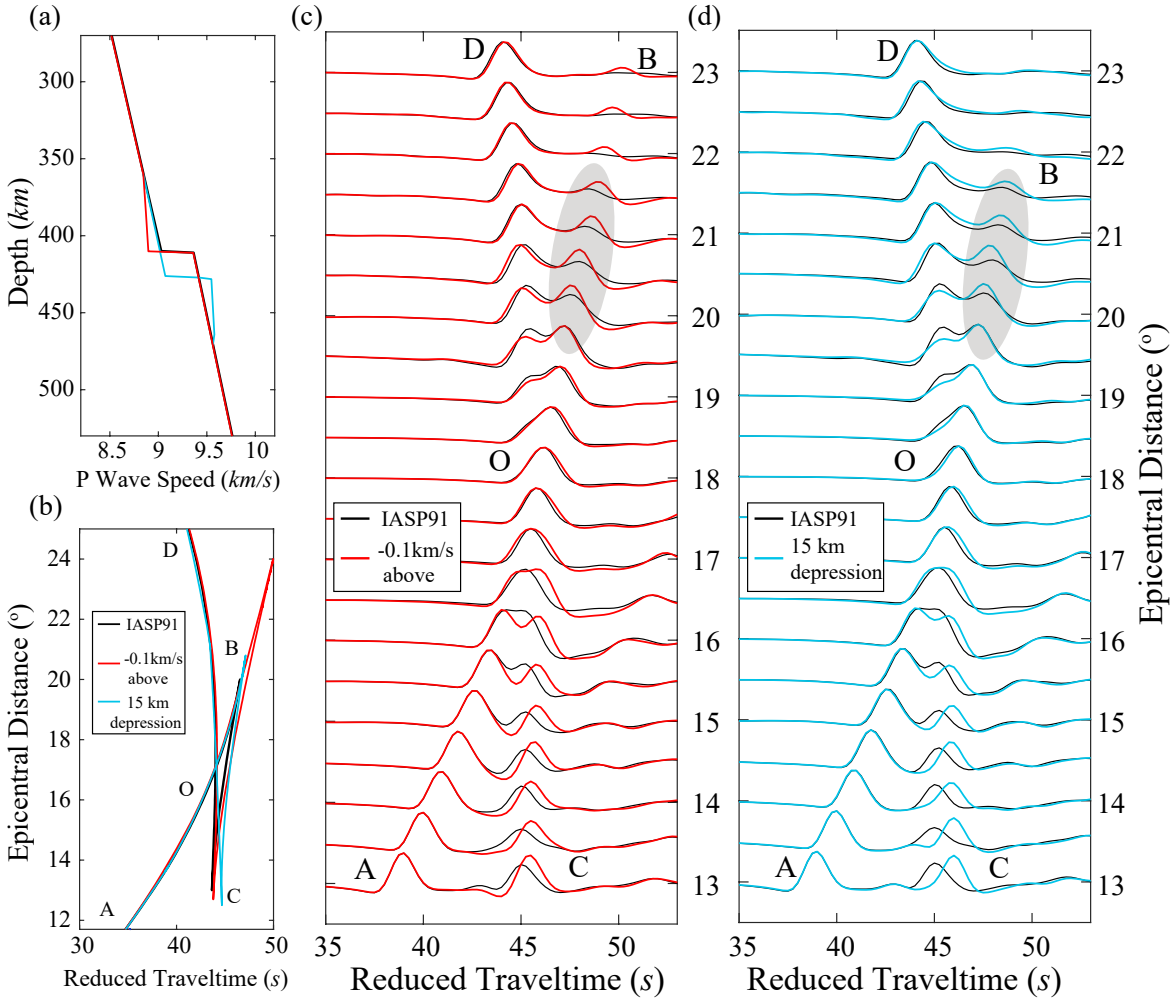

Figure 2. Modeling tests for the tradeoff between the low wave speed zone above the interface and a depressed interface. (a) The black line shows the IASP91 model (Kennett & Engdahl 1991), the red line shows the model with a low wave speed zone above the discontinuity, and the blue line is the model with a 15-km depression for the discontinuity. (b) Travel time curves for the corresponding models in (a) with the same color. AB, BC, and CD indicate direct, reflected, and refracted waves, respectively. O denotes the crossover point of the AB and CD branch. (c) Waveform comparison between the IASP91 model (black) and the model with a low wave speed zone above the discontinuity (red). The amplitude is normalized by each trace and the most obvious difference is the increased amplitude near the cusp B. (d) Waveform comparison between the IASP91 model (black) and the model with a 15-km depression for the discontinuity (blue). The amplitude is normalized by each trace and amplitude near the cusp B is also increased.

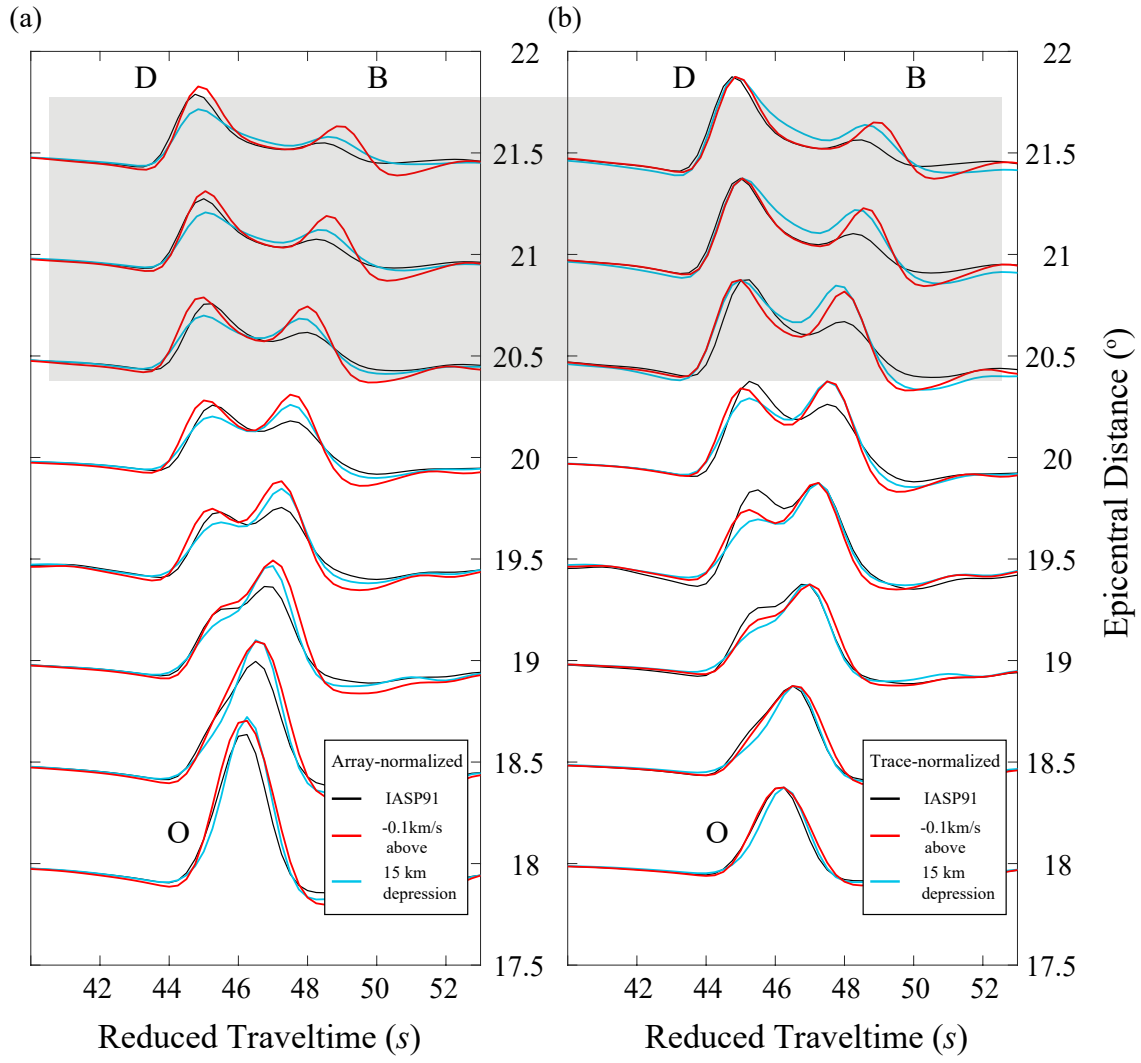

Figure 3. Using array normalization to minimize the tradeoff between model parameters. (a) Array-normalized waveforms. Black waveforms are for the IASP91 model (black line in Fig. 2b), red waveforms are for the model with a low wave speed zone above the discontinuity (the red line in Fig. 2b), and blue waveforms are the model with a 15-km depression for the discontinuity (the blue line in Fig. 2b). Differences between the two model types (the red and blue line in Fig. 2b) are clearly shown in the relative amplitude variations between stations (in the shaded grey region). (b) Trace-normalized waveforms. Symbols are the same as (a) and the shaded grey area shows where both the amplitude for OB and OD branch is magnified due to trace normalization. Therefore, no obvious differences exist and tradeoff occurs.

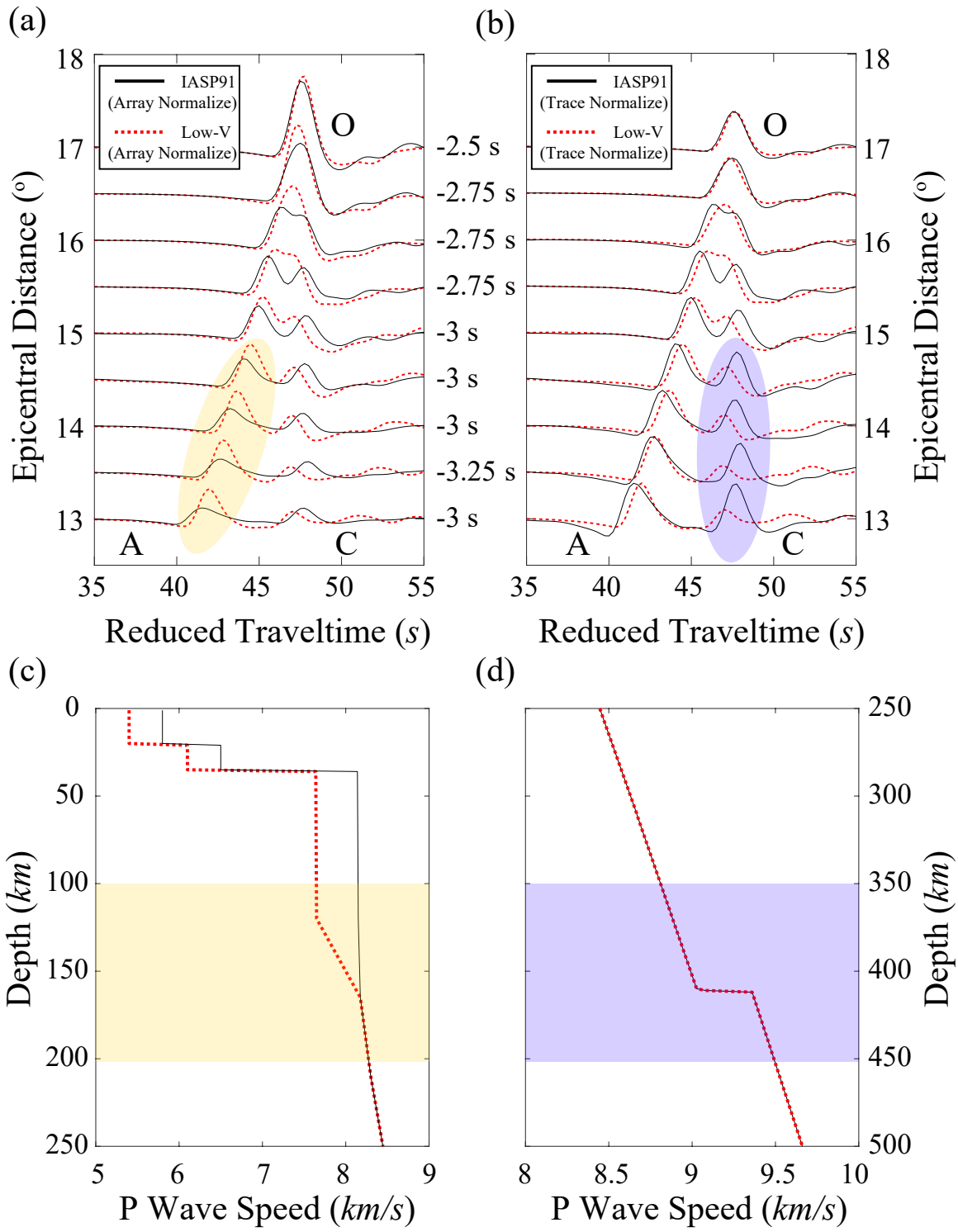

Figure 4. Misinterpretation of the anomaly caused by the trace normalization. (a) Array-normalized waveforms. Solid black waveforms are synthetics for the IASP91 model (Kennett & Engdahl 1991) and dotted red waveforms are for the red model in (c). The yellow region shows where the amplitudes are different. The number near the end of each trace denotes the time delay ($\sim$ 3 s) for each station. (b) Trace-normalized waveforms. Blue dashed oval shows where the waveforms are different. (c) The shallow portion of the model. The solid black line is the IASP91 model, and the dotted red line is the designed model with a -0.4km/s zone in the top 160 km. The yellow box shows where the wave speed gradient changes. (d) The deep portion of the model. The blue box roughly shows where we tend to modify when applying the trace normalization.

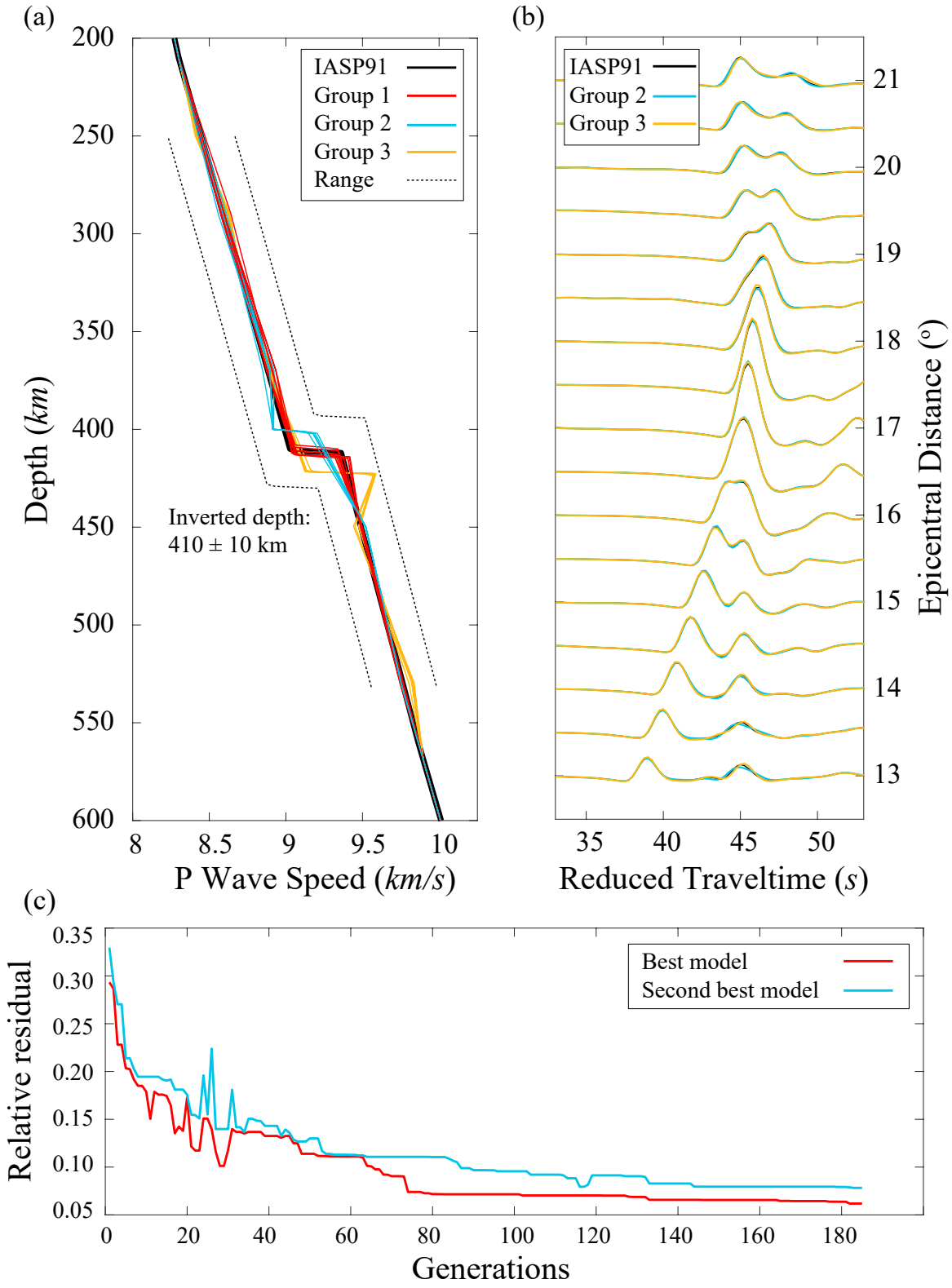

Figure 5. Synthetic tests for Niche Genetic Algorithm. (a) Inverted models. The solid black line is the IASP91 model (Kennett & Engdahl 1991). Red, blue, and yellow lines show different groups of the acceptable models. The dotted black lines represent the model searching range. (b) Waveform fitting. Black waveforms are synthetics for the IASP91 model, blue waveforms are synthetics for one of the models from model group two, and yellow waveforms are synthetics for one of the models from model group three. (c) Residual between data and synthetics with respect to generations. The red and blue lines are the residual for the best and second-best models, respectively.

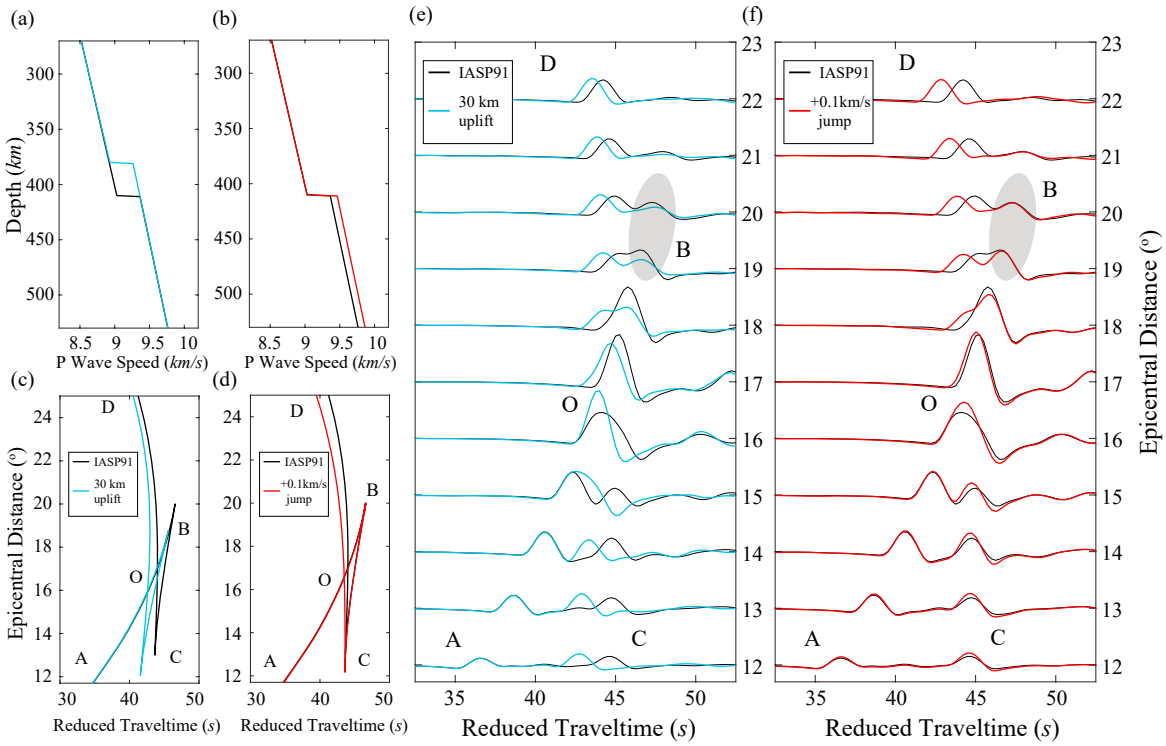

Figure 6. Modeling tests for the influence of topography and wave speed jump on the triplications. (a) The black line shows the IASP91 model (Kennett & Engdahl 1991), whereas the blue line is the model with a 30-km uplift for the 410-km discontinuity. (b) The black line shows the IASP91 model, whereas the red line is the model with a +0.1 km/s wave speed jump across the 410-km discontinuity. (c) Travel time curves for the IASP91 model (black line) and the model with a 30-km uplift (blue line). AB, BC, and CD indicate direct, reflected and, refracted waves, respectively. O denotes the crossover point of the AB and CD branch. (d) Travel time curves for the IASP91 model (black line) and the model with a +0.1 km/s wave speed jump across the 410-km discontinuity (red line). (e) Waveform comparison between the model with a 30-km uplift (blue) and the IASP91 model (black). A reducing slowness of 11 s/^{o} is used for the time plot. (f) Waveform comparison between the model with a +0.1km/s wave speed jump across the 410-km discontinuity (red) and the IASP91 model (black).

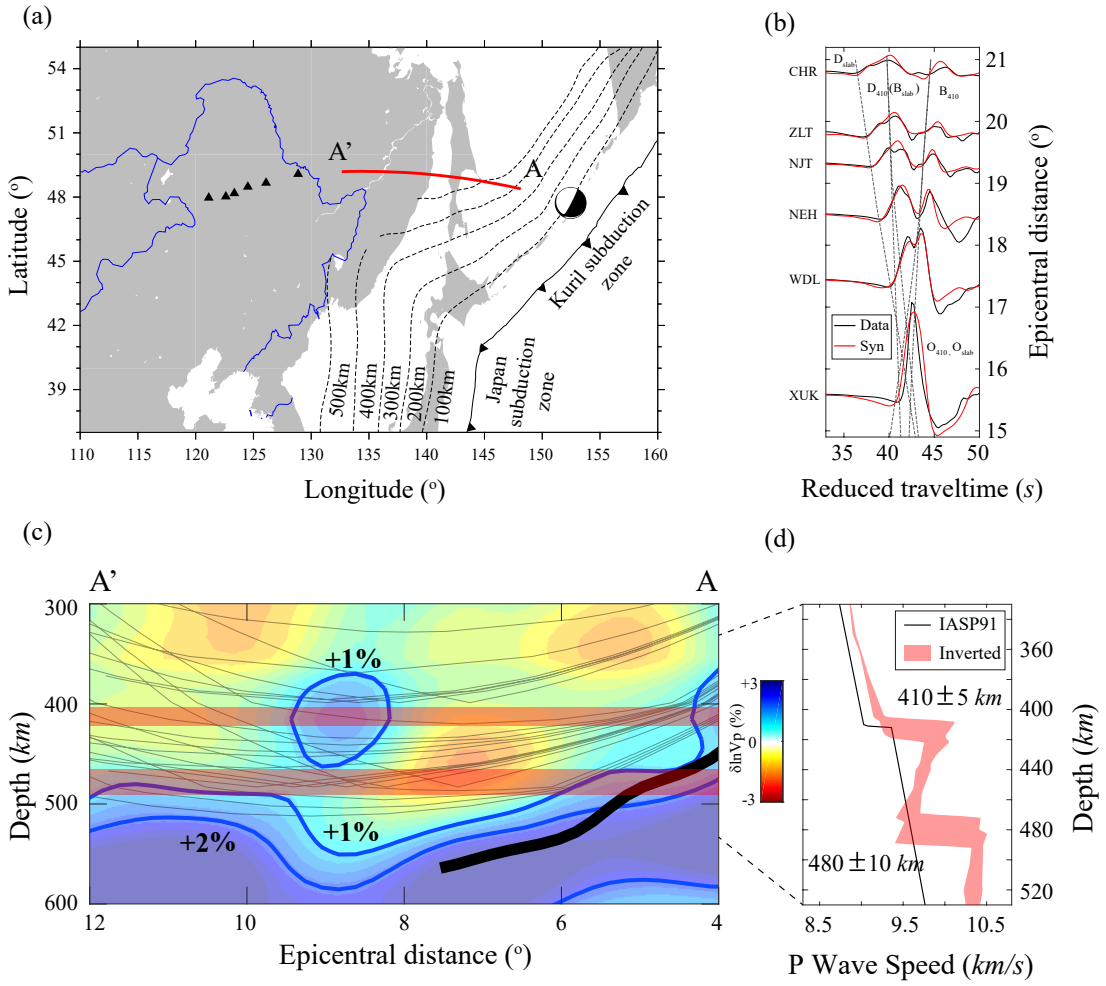

Figure 7. Research region and inversion results. (a) Research region and the distribution of stations and the event. The black beach ball and black triangles represent the event and stations respectively. The red line shows the location of the cross-section AA' in (c). Black dashed lines are the depth contours of the subduction zone, with numbers showing the corresponding depths. (b) Displacement waveform comparison between data and synthetics in the vertical component for P wave. A reducing slowness of 11 s/^{o} is used for the time plot. For each trace, the station name is given on the left. The red waveform is the synthetic waveform from one of the inverted models. The black waveform is the recorded waveform after alignment with the synthetic one by cross-correlation. And dashed grey lines show the corresponding travel-time curves calculated by Taup Toolkit (Crotwell et al. 1999). $O_{410}B_{410}$ and $O_{slab}B_{slab}$ represent the direct waves above the 410-km, and the upper slab surface, respectively. $O_{410}D_{410}$ and $O_{slab}D_{slab}$ represent the refracted wave below these interfaces. (c) Cross-section AA' as shown in (a). The background is from the FWEA18 tomography model (Tao et al. 2018), and the blue lines are its wave speed contours. The bold black line is the location of the slab upper surface from the Slab2.0 model (Hayes et al. 2018). The grey lines are the ray paths. And the shaded red regions are the locations of the inverted interfaces with uncertainties. (d) P wave speed inversion results. The shaded red region shows all the inverted acceptable models, whereas the black line indicates the IASP91 model (Kennett & Engdahl 1991). This depth range from 330 km to 530 km is the most reliable region where the ray paths (grey lines) are dense enough as shown in (c).

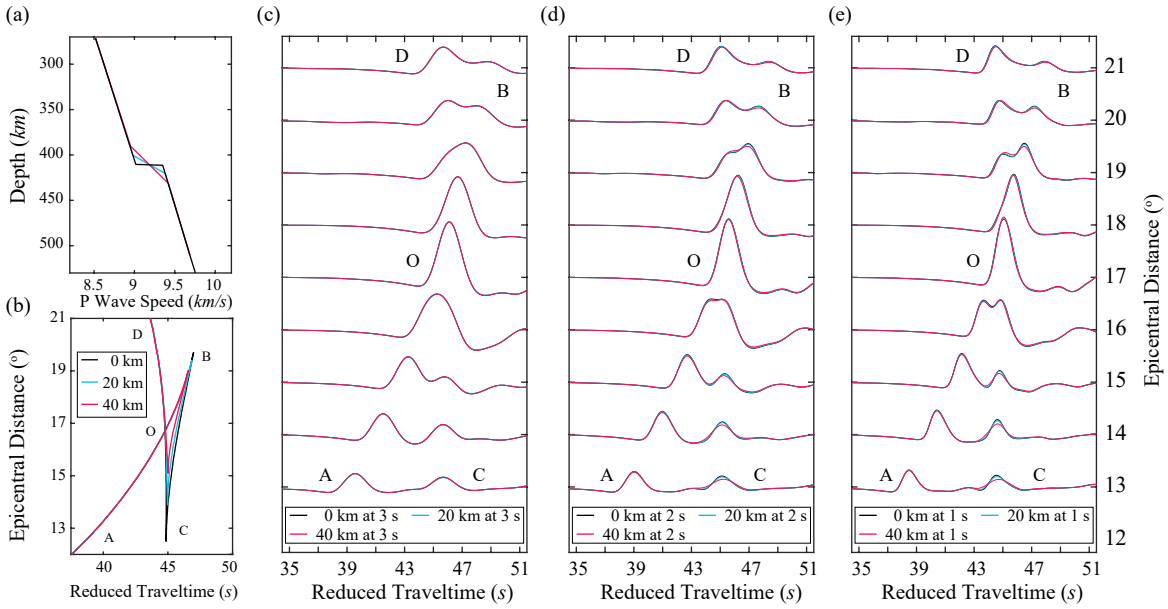

Figure 8. Modeling tests for the effect of the sharpness of the interface on the triplications. (a) Models used in the synthetic test. The black line is the IAPS91 model (Kennett & Engdahl 1991), while the blue and red lines are models in which the 410-km discontinuity is replaced by a gradual transition with thicknesses of 20 km and 40 km, respectively. (b) The corresponding travel time curves which are plotted in the same color as the models in (a). (c) Synthetic waveforms corresponding to models of the same colors in (a). Although there are significant differences in the travel time curves as shown in (b), the waveforms are almost the same with a period of 3 s. (d) Synthetic waveforms comparison with a period of 2 s. (e) Synthetic waveforms comparison with a period of 1 s. We should note that for all these cases, a $t^* \sim 1$ s is applied.

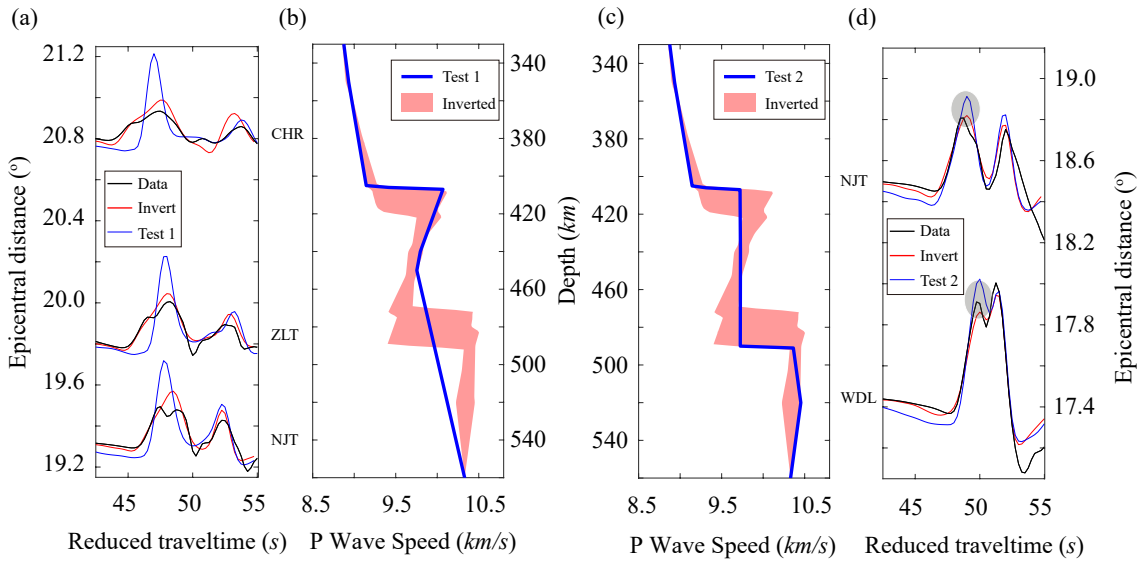

Figure 9. Validation for the inverted model. (a) Waveforms comparison between the model with and without the slab upper surface. The black waveforms are the data, the red waveforms are from the model with both the 410-km discontinuity and the upper slab surface, and the blue waveforms are from the model with only the 410-km discontinuity. (b) The shaded red region indicates the inverted acceptable models, and the blue model has only one interface. (c) The shaded red region marks the inverted models with a more substantial wave speed jump across the 410-km discontinuity and a low wave speed anomaly above the slab upper surface, and the blue model has an averaged wave speed between these two interfaces. (d) Waveforms comparison between the model with and without the low wave speed anomaly. The black waveforms are the data, the red waveforms are from the model with the low wave speed anomaly, and the blue waveforms are from the model with a relatively normal wave speed gradient. In the shaded grey area, the amplitudes of the blue waveforms are $\sim$ 10-20% larger than the records.